Published in final edited form as:
IEEE Trans Med Imaging. 2006 February ; 25(2): 198–209. doi:10.1109/TMI.2005.862205.

Observer efficiency in discrimination tasks simulating malignant and benign breast lesions imaged with ultrasound

Craig K. Abbey,
Dept. of Biomedical Engineering, University of California at Davis and the Dept of Psychology, University of California at Santa Barabara, Santa Barbara, CA 93106 USA (phone: 805-893-3853; fax: 805-893-4303; e-mail: abbey@psych.ucsb.edu).

Roger J. Zemp,
Department of Biomedical Engineering, Texas A&M University, College Station. USA (e-mail: rjzemp@tamu.edu).

Jie Liu,
Dept. of Bioengineering, University of Illinois at Urbana-Champaign. USA (e-mail: liujie@uiuc.edu).

Karen K. Lindfors, and
Dept. of Radiology, UC Davis Medical Center, Sacramento California. USA (e-mail: karen.lindfors@ucdmc.ucdavis.edu).

Michael F. Insana
Dept. of Bioengineering, University of Illinois at Urbana-Champaign. USA (e-mail: mfi@uiuc.edu).

Abstract

We investigate and extend the ideal observer methodology developed by Smith and Wagner to detection and discrimination tasks related to breast sonography. We provide a numerical approach for evaluating the ideal observer acting on radio-frequency (RF) frame data, which involves inversion of large nonstationary covariance matrices, and we describe a power-series approach to computing this inverse. Considering a truncated power series suggests that the RF data be Wiener-filtered before forming the final envelope image. We have compared human performance for Wiener-filtered and conventional B-mode envelope images using psychophysical studies for 5 tasks related to breast cancer classification. We find significant improvements in visual detection and discrimination efficiency in four of these five tasks. We also use the Smith-Wagner approach to distinguish between human and processing inefficiencies, and find that generally the principle limitation comes from the information lost in computing the final envelope image.

Index Terms

Breast Sonography; ideal observer; image quality; Wiener filter

I. INTRODUCTION

The objective approach to assessment of image quality utilizes task performance as the figure of merit for determining medical image quality [1]. In this way, all components of the imaging chain - from the formation of contrast in the body to display and reader effects - can be investigated for their influence on diagnostic accuracy. For analyzing imaging systems, it can be illuminating to consider the performance of the Bayesian ideal observer [2] - often referred to simply as the ideal observer. The ideal observer yields optimal task performance and therefore serves as a measure of the task-relevant information content of the data [3],

which has direct application for system optimization. In addition to identifying imaging devices or configurations that maximize diagnostic information, ideal observer analysis can be used to identify loss of information in components such as image processing, display and interpretation. This is done by looking at a relative measure of task performance – referred to as efficiency - between the end user and the ideal observer on the raw acquired data. The limitation of the ideal observer approach is that it requires complete statistical knowledge of the images under consideration, which is not feasible in a clinical environment. However, ideal observer analysis is well suited for controlled simulation studies used to investigate new technologies and processing methodologies [4].

In a series of highly regarded articles [5–7], Smith, Wagner, and coworkers described such an approach for ultrasonic imaging of backscattered acoustic energy. They used an ideal-observer approach to rigorously show the role of speckle size (i.e. system resolution) on detectability of large low-contrast lesions in the presence of fully developed speckle. Their approach introduced task-based assessment of image quality to the ultrasound community and has guided much subsequent investigation of ultrasonic image quality including this work.

We have been investigating this approach to analyze ultrasonic signal processing before computation of the final envelope image [8–11]. Modern ultrasound systems have the ability to digitize and store radio-frequency (RF) or demodulated signals [12]. This allows for increased flexibility in processing the image data before computing the final envelope image. These systems also operate at higher frequencies yielding greater bandwidth for possible enhancement. In addition, there is currently great interest in coded excitation that requires “decoding” at the RF level [13]. Like Smith and Wagner [5,6], we assume Gaussian distributions for acoustic scattering in tissue, which implies fully developed speckle, and we assume a isoplanatic region leading to a shift-invariant focused pulse. However, we explicitly include Gaussian electronic noise in the signal acquisition stage, and we investigate discrimination tasks in addition to low-contrast detection.

Our rationale for considering discrimination tasks comes from clinical applications of ultrasonic imaging to discriminate malignant breast lesions from benign [14]. Sonography is generally used as an adjunct to mammography in women with suspicious findings [15], where it has been found to increase sensitivity (observed increases from 83% to 91% [16] and from 74% to 97% [17]) without significantly reduced specificity. Sonography has also been suggested as a screening modality in women with mammographically dense breasts [17–19] where observed sensitivity is approximately 75% [17].

An advantage of working in the sampled RF domain is that the signal is well modeled as a noisy linear transformation of the object scattering function, and thus by our assumptions can be described by correlated multivariate Gaussian distributions. The ideal observer decision variable in simple detection and discrimination tasks is therefore given by a quadratic function of the RF data that involve the inverse of RF covariance matrices [20]. Although the ideal observer's decision variable is well defined, evaluating the ideal observer remains a computational challenge due to the necessity of inverting large nonstationary covariance matrices.

We have been able to successfully accomplish the necessary covariance-matrix inversion for detection tasks through the use of a power series expansion [8]. Here we derive and extend that approach to discrimination tasks designed to simulate the differentiation of malignant from benign breast tissue. We also show how truncating the power series after the first iteration is equivalent to application of a Wiener filter to the RF frame data before computing an envelope image. A number of researchers have addressed the possibility of

improving ultrasonic imaging through deconvolution of the RF signal before computing the B-mode envelope [21,22]. Our approach suggests the Wiener filter instead of a more standard inverse filter, and places this filter in the context of an optimal decision variable.

In this work, we evaluate Wiener-filtering and standard B-mode processing for a panel of five tasks related to detecting and discriminating malignant from benign breast tissue. We investigate ideal observer performance on these tasks through Monte-Carlo studies, and we investigate human observers through psychophysical studies. Comparing the efficiency of human-observer performance in B-mode and Wiener-filtered envelope images allows us to quantify improvements in task performance relative to the amount of diagnostic information available in the RF data. As shown below, human observer efficiency with respect to the ideal observer varies considerably across tasks. It is therefore of interest to know if this reflects information lost in the computation of an envelope image or if it reflects limitations in human-observers' ability to extract information from the envelope image. To examine this question, we use a model observer based on the Smith-Wagner approach to analyze the envelope images. By comparing the efficiency of the Smith-Wagner observers to the efficiency of the human observers we gain insight into where diagnostic information is lost in the transformation from an RF frame to the final envelope image.

II. THEORY

In this section we consider a model of image formation in ultrasound that is based on the idea of linear operators acting on Gaussian stochastic processes. A graphical depiction of this model is given in Figure 1. Since the goal is to analyze two class discrimination tasks, we develop in this model with different variance profiles depending on whether malignant or benign tissue is present.

A. System modeling

We begin by modeling scattering properties of tissue as a zero-mean Gaussian stochastic process that gives rise to incoherent scattering [23]. Samples from a 2-D scattering functions representing the object being imaged can be arranged into a column vector **f** by lexicographical reordering. In this work we will not consider specular reflections, but we note that this phenomenon could be included through the use of a nonzero mean object.

Let H_1 indicate the hypothesis that **f** represents scattering from a benign focal lesion, and H_2 be the hypothesis that f is from a malignant lesion. We assume that the spatial distribution of scattering from either type of tissue can be modeled using multivariate normal (MVN) distributions, and that the distributions have a common scattering variance, σ^2_{obj}, that characterizes the overall magnitude of scattering in the tissue. However, we allow each hypothesis a unique pattern of departure from this variance, encoded in diagonal deviation matrices $\mathbf{S}_1$ and $\mathbf{S}_2$. The distribution of **f** under each hypothesis is thus given by

$$\begin{aligned} H_1{:}\mathbf{f} &\sim \text{MVN}\left(\mathbf{0}, \sigma^2_{\text{obj}}(\mathbf{I}+\mathbf{S}_1)\right) \\ H_2{:}\mathbf{f} &\sim \text{MVN}\left(\mathbf{0}, \sigma^2_{\text{obj}}(\mathbf{I}+\mathbf{S}_2)\right). \end{aligned} \tag{1}$$

The diagonal elements of $\mathbf{S}_1$ and $\mathbf{S}_2$ can be positive or negative, but they must be greater than −1 to preserve positivity of the variance. A number of choices for these two matrices can be found below in Figure 2.

The next step of the modeling process, the creation of radio-frequency (RF) data from the scattering object, can be implemented as a noisy linear transformation of the scattering object

$$\mathbf{g}=\mathbf{H}\mathbf{f}+\mathbf{n}, \tag{2}$$

where **g** is the vector of RF frame data, **H** is the system matrix characterizing the transformation, and **n** is object independent system noise that arises in the detection process. The system noise is assumed to be a zero-mean Gaussian white-noise process with variance σ^2_n. The resulting statistical model for the RF frame is given by

$$\begin{aligned} H_1{:}\mathbf{g} &\sim \mathrm{MVN}(\mathbf{0}, \boldsymbol{\Sigma}_1) \\ H_2{:}\mathbf{g} &\sim \mathrm{MVN}(\mathbf{0}, \boldsymbol{\Sigma}_2), \end{aligned} \tag{3}$$

where

$$\boldsymbol{\Sigma}_i=\sigma^2_{\mathrm{obj}}\mathbf{H}\,(\mathbf{I}+\mathbf{S}_i)\,\mathbf{H}^t+\sigma^2_n\mathbf{I},\ i=1,2. \tag{4}$$

Nondiagonal and nonstationary covariance matrices under the two hypotheses arise from the propagation of nonstationary variance in Equation (1) through the noisy linear transformation in Equation (2). All information about the object and imaging system is contained in $\boldsymbol{\Sigma}_i$.

Our analysis of the ideal observer is tailored to RF frames of echo data. However, to complete the process for the purpose of creating an image, the final step of image formation is demodulation and envelope computation [24]. The demodulation step can be implemented by multiplying **g** with a complex exponential along each axial scan line, followed by low pass filtering and computation of the magnitude. For example, an envelope image is derived from a frame of RF data, **g**, by the computation

$$\mathbf{b}=|\mathbf{L}\mathbf{M}\mathbf{g}|, \tag{5}$$

where **M** is a diagonal "mixing" transform that implements multiplication with a complex exponential tuned to the carrier frequency of the pulse, and **L** is a lowpass filtering matrix that removes undesirable harmonic frequencies, and yields in-phase (I) and quadrature (Q) signals as the real and imaginary parts of a complex signal. The magnitude of this signal is computed on an element-by-element basis by the | | brackets. Computing the echo envelope is non-linear and, as a result, makes the full multivariate distribution of the resulting envelope image difficult to analyze without imposing assumptions [5,6]. Downsampling the echo data without aliasing will not alter the information content of the envelope image, and therefore is ignored in our analysis.

B. Ideal observer

The ideal observer test statistic for binary discrimination tasks is conventionally defined by the ratio of the probability density function (PDF) for H_2 to that of H_1. Equivalently, one can use the logarithm of this and ignore terms unrelated to the data. For the Gaussian distributions of the form given in Equation (3), the resulting log-likelihood-ratio decision variable is given by

$$\lambda(\mathbf{g})=\mathrm{Ln}\left(\frac{p_2(\mathbf{g})}{p_1(\mathbf{g})}\right) \simeq \frac{1}{2}\mathbf{g}^t\,(\boldsymbol{\Sigma}_1^{-1}-\boldsymbol{\Sigma}_2^{-1})\,\mathbf{g}. \tag{6}$$

A high value for this variable indicates greater likelihood for H_2 while a low value indicates greater likelihood for H_1. Because the object contrast only produces differences in the covariance matrix of **g** under the two hypotheses, the decision variable is quadratic in the echo data [20, 25]. As described below, this test statistic can be used in Monte-Carlo studies

to evaluate ideal observer performance in binary discrimination tasks. However, for this approach to be implemented, a computational issue that must be addressed in Equation 6 is efficient computation of matrix vector products involving $\boldsymbol{\Sigma}_i^{-1}$ which are generally too large to be computed through straightforward numerical inversion.

C. Power series inversion

To resolve the matrix inversion problem, we propose a power-series approach to computing matrix-vector products with inverse covariance matrices. Our method relies on the decomposition of the image covariance matrices into stationary and nonstationary components. This requires the additional assumption that the impulse response of the imaging system (i.e., rows of the system matrix, **H**) be shift invariant. Consequently **H** is a circulant matrix, the product **Hf** is a discrete convolution, and hence the approach is limited to isoplanatic regions. The assumption of shift-invariance allows us to diagonalize **H** by a Fourier transform,

$$\mathbf{H}=\mathbf{F}^{-1}\mathbf{T}\mathbf{F}, \tag{7}$$

where **F** is the 2-D forward Finite Fourier-Transform matrix, and **T** is a diagonal matrix whose elements are the eigenvalues of **H** and also the Fourier transform of the system impulse response [25,26]. We use a unitary implementation of the Finite Fourier Transform to avoid keeping track of scaling constants; hence the inverse Fourier transform is also the adjoint of the forward transform, $\mathbf{F}^{-1} = \mathbf{F}^{\dagger}$ [25].

The power series approach to inversion of a matrix is incorporated in the relationship [27]

$$(\mathbf{I}-\mathbf{A})^{-1}=\sum_{k=0}^{\infty}\mathbf{A}^k,$$

which holds if the eigenvalues of **A** are between −1 and 1 (this form is reminiscent of the limit of a geometric series). In terms of the RF covariance matrices, we can write each covariance matrix as

$$\begin{aligned}\boldsymbol{\Sigma}_i &= \sigma_{\text{obj}}^2\mathbf{H}\mathbf{H}^t+\sigma_n^2\mathbf{I}+\sigma_{\text{obj}}^2\mathbf{H}\mathbf{S}_i\mathbf{H}^t \\ &= \boldsymbol{\Sigma}_0+\boldsymbol{\Delta\Sigma}_i,\end{aligned} \tag{8}$$

where $\boldsymbol{\Sigma}_0$ is the stationary component comprised of the first two terms on the right side of line 1, and $\boldsymbol{\Delta\Sigma}_i$ is the nonstationary component that is dependent on the variance profile, $\mathbf{S}_i$. The stationary component happens to be common to both hypotheses and is therefore independent of *i*. Similar to Equation 7, the stationary assumption allows us to diagonalize $\boldsymbol{\Sigma}_0$ by a Fourier transform,

$$\boldsymbol{\Sigma}_0=\mathbf{F}^{-1}\mathbf{N}_0\mathbf{F}, \tag{9}$$

where the diagonal matrix, $\mathbf{N}_0$, is the power spectrum corresponding to $\boldsymbol{\Sigma}_0$. The diagonal elements of $\mathbf{N}_0$ are given by

$$[\mathbf{N}_0]_{ii}=\sigma_{\text{obj}}^2\left|[\mathbf{T}]_{ii}\right|^2+\sigma_n^2,$$

where **T** is the transfer function of **H** as defined in Equation 7.

The decomposition in Equation 8 allows us to write the covariance matrix in a form amenable to power series inversion,

$$\boldsymbol{\Sigma}_i = \boldsymbol{\Sigma}_0^{1/2} \left(\mathbf{I} + \boldsymbol{\Sigma}_0^{-1/2} \boldsymbol{\Delta\Sigma}_i \boldsymbol{\Sigma}_0^{-1/2}\right) \boldsymbol{\Sigma}_0^{1/2}.$$

The resulting form for the inverse of the covariance matrix is given by

$$\begin{aligned} \boldsymbol{\Sigma}_i^{-1} &= \boldsymbol{\Sigma}_0^{-1/2} \left(\mathbf{I} + \boldsymbol{\Sigma}_0^{-1/2} \boldsymbol{\Delta\Sigma}_i \boldsymbol{\Sigma}_0^{-1/2}\right)^{-1} \boldsymbol{\Sigma}_0^{-1/2} \\ &= \boldsymbol{\Sigma}_0^{-1/2} \left(\sum_{k=0}^{\infty} \left(-\boldsymbol{\Sigma}_0^{-1/2} \boldsymbol{\Delta\Sigma}_i \boldsymbol{\Sigma}_0^{-1/2}\right)^k \right) \boldsymbol{\Sigma}_0^{-1/2}. \end{aligned} \tag{10}$$

Note that the stationary components of this expression, the $\boldsymbol{\Sigma}_0^{-1/2}$ factors, can be computed readily using the Fourier methods described above. They consist of a Fourier Transform, division by the square-root of the RF power spectrum, $\mathbf{N}_0$, and an inverse Fourier transform. As we describe below, Equation 10 can be implemented iteratively to get the quadratic forms in Equation 6 presuming that conditions for convergence have been met.

D. Iterative implementation of the power series

The power series in Equation 10 can be implemented more efficiently through an iterative procedure. In the Monte-Carlo studies described below, we will need to compute quadratic products of the form $\mathbf{g}^t \boldsymbol{\Sigma}_i^{-1} \mathbf{g}$, where the vector $\mathbf{g}$ is a frame of (simulated) RF data lexicographically indexed as a vector. Assuming convergence of the power series, we can approximate this product with the first K elements of the summation in Equation 10. The iteration begins by initializing two vectors, $\mathbf{u}_0 = \mathbf{v}_0 = \boldsymbol{\Sigma}_0^{-1/2} \mathbf{g}$, and then iterating

$$\begin{aligned} \mathbf{u}_j &= -\boldsymbol{\Sigma}_0^{-1/2} \boldsymbol{\Delta\Sigma}_i \boldsymbol{\Sigma}_0^{-1/2} \mathbf{u}_{j-1}, \\ \mathbf{v}_j &= \mathbf{v}_{j-1} + \mathbf{u}_j, \end{aligned} \tag{11}$$

for $j = 1$ to K. The quadratic form is then approximated by the inner product $\mathbf{v}_0^t \mathbf{v}_K$. The proof of this algorithm is given in the Appendix.

E. Wiener filter

The Wiener filter in imaging is typically derived from a consideration of blurring and noise effects on images [26,28]. We will show how the filter emerges from the quadratic form in Equation 6 by truncating the power series inversion in Equation 10.

If we truncate the power series expansion at $k = 1$, we obtain the following approximation for the difference in inverse covariance matrices,

$$\boldsymbol{\Sigma}_1^{-1} - \boldsymbol{\Sigma}_2^{-1} \approx \boldsymbol{\Sigma}_0^{-1} \left(\boldsymbol{\Delta\Sigma}_1 - \boldsymbol{\Delta\Sigma}_2\right) \boldsymbol{\Sigma}_0^{-1}.$$

Substituting this into Equation 6 yields an approximation to the ideal-observer test statistic of

$$\lambda(\mathbf{g}) \approx \frac{\sigma_{\text{obj}}^2}{2} \mathbf{g}^T \boldsymbol{\Sigma}_0^{-1} \mathbf{H} \left(\mathbf{S}_2 - \mathbf{S}_1\right) \mathbf{H}^T \boldsymbol{\Sigma}_0^{-1} \mathbf{g}. \tag{12}$$

Terms of the form $\sigma_{\text{obj}}^2 \mathbf{H}^T \boldsymbol{\Sigma}_0^{-1} \mathbf{g}$ are recognizable as a Wiener-filtered version of the RF frame [26]. Equation 12 suggests that Wiener filtering in the RF domain before computing an envelope may capture important components of the ideal observer test statistic. Demodulation and envelope computation, performed after Wiener-filtering, can be used to compute an image as described in Equation 5. Appearance of the Weiner filter in Equation 12 raises the question: Can Wiener filtering of RF echo data improve our efficiency for visual detection and discrimination?

F. Smith-Wagner envelope observers

As we have described in the introduction, Smith, Wagner and co-workers [5–7] have analyzed low-contrast lesion detectability for medical ultrasonic imaging using envelope image data. The basis of the Smith-Wagner approach is the notion of an observer decision variable that is computed as a weighted sum of the envelope intensity,

$$\lambda_{\text{sw}}(\mathbf{b}) = \sum_i a_i b_i^2 = \mathbf{a}^t \mathbf{b}^2, \tag{13}$$

where the a_i are elements of a vector of weights, and the b_i are samples of the echo envelope as in Equation 5. Samples are squared on an element-by-element basis to obtain the envelope intensity at each point.

Smith and Wagner argued [6] from the basis of laser speckle statistics described by Goodman [5,29] that Equation 13 can closely approximate the decision variable of the ideal observer acting on envelope images for the task of detecting of a focal deviation in scattering intensity. To make this argument, they assumed the contrast within the focal deviation (i.e. the lesion) was constant and small, so that statistical properties of the envelope data were approximately stationary. Also, they assumed the lesion area was relatively large, at least 10 times the speckle correlation area, because their analysis was for contrast limited rather than spatial resolution limited detection tasks. In this case, the elements of **a** are constant in the focal region and zero outside of this region. In terms of the scattering deviation matrices defined in Equation 1, the Smith-Wagner decision variable can be written as

$$\lambda_{sw}(\mathbf{b}) = \mathbf{b}^t (\mathbf{S}_2 - \mathbf{S}_1) \mathbf{b}. \tag{14}$$

We will employ this decision variable as an approximation to the ideal observer acting on envelope images, including envelope images derived from Wiener-filtered RF frames. This application requires an additional assumptions since the approach was derived for low-contrast large area detection tasks, and here we are applying it, in some cases, to small-area high-contrast discrimination tasks. We discuss the implications of this below in Section IV.

III. METHODS

Comparing the performance of the ideal observer on RF data with the Smith-Wagner result for envelope-detected data allows us to test the notion that computation of a B-mode envelope image may result in a significant loss of diagnostic information, and that at least some of that information may be retained by first Wiener filtering the RF data. To this end, we have designed a panel of visual tasks related to detecting and discriminating malignant and benign tissue in breast lesions. We then simulate the acquisition of RF data using parameters derived from a clinical ultrasound scanner. This simulation procedure is used to assess the performance of the RF ideal observer, of Smith-Wagner approximations to

envelope-image ideal observers for B-mode and Wiener-filtered envelope images, and for trained human observers.

A. Experiments

We have proposed five detection tasks based on candidate features that trained experts are likely to look for in the process of detecting and discriminating malignant from benign breast lesions with ultrasound [14]. The specific scattering objects used in the simulation are defined by their variance profiles and are classified as either “malignant” or “benign” as shown in Figure 2. We also display the difference between the two variance profiles since this defines the contrast between the two hypotheses, and is a critical component of the test statistic in Equation 12. The five tasks considered represent detection of a hypoechoic lesion (Task 1), discrimination of an elongated eccentric lesion from a circular lesion (Task 2), discrimination of a soft, poorly defined boundary from a well-circumscribed lesion (Task 3), discriminating boundary irregularities from a smooth boundary (Task 4), and discriminating hypoechoic from anechoic lesion interiors (Task 5).

The difficulty of each task is controlled through a parameter that governs the difference between the variance maps for H_1 and H_2. Increasing this parameter in each case makes the task easier to perform. For Task 1, this controlling parameter is the contrast of the lesion [30]. For Task 2, it is the eccentricity of the lesion. For Task 3, it is the width of a Gaussian blurring kernel that smoothes the lesion variance map to give it a soft boundary. In Task 4 the controlling parameter is the length that irregularities deviate from a circular boundary. Task 5 is parameterized by the difference in the interior contrast of the lesions.

The parameters relate the variance map to physical properties of a lesion, but they are unwieldy for comparisons between tasks. For example, it is not clear how the eccentricity used in Task 2 relates to interior scattering contrast in Task 5. To place all tasks on a common scale, we define an object contrast factor as the integrated absolute value of the variance deviation profiles,

$$C = \sum_i |[\mathbf{S}_2 - \mathbf{S}_1]_{ii}| \Delta x \Delta y, \tag{15}$$

where Δx and Δy are RF sampling intervals in the axial and lateral directions. Recall from Equation 1 that the deviation matrices are diagonal, and hence the sum need only be computed over the diagonal elements. The parameters described above are used to generate two object variance profiles for a given experiment, and from these the object contrast factor of the experiment is defined. We report ideal-observer performance values as a function of the object contrast factor defined in Equation 15.

B. Echo signal model

The experiments described below were based on images generated using a Sonoline Elegra Ultrasound System with a 7 MHz linear array (Siemens Medical Solutions, Mountain View, CA). The system provides baseband in-phase and quadrature echo data with a 12 MHz bandwidth that is sampled at 36 Msamples/s. These signals are down sampled by a factor of 2.5 before file transfer and then up sampled as needed for analysis. We modeled the point spread function of the system after this experimental system to determine the **H** matrix introduced in Equation 2. The transmission carrier frequency was 7.2 MHz. The Gabor-function pulse was simulated with a percent bandwidth of 51.7% (full width at half max) and a peak signal power to noise power echo SNR of 45.5dB. The pulse parameters were derived from previous studies using a line reflector in an agar block [31]. The 2-D simulated pulse profile shown in Figure 3 can be thought of as one row of the **H** matrix.

Variance profiles from the top two rows of Figure 2 were used to generate realizations of the random object scattering vector, **f** (left side of Figure 1) via pseudo-random number sequences and Equation 1. Noisy RF echo signals were then found by applying Equation 2. Examples of B-mode and Wiener filtered images generated with this procedure can be seen in Figure 4. The speckle texture of the B-mode images is qualitatively similar to what is found in breast sonograms. However, at this stage, the model does not allow for many of the inhomogeneities of normal breast tissue such as layers of fatty tissue, ducts, Cooper's ligaments, and fibroglandular tissue [14]. This makes the region outside the lesion more uniform than what is found in clinical sonograms. The lesion itself is also more regular (round) than clinical lesions, reflecting the fact that the model does not at this stage accommodate variable lesion shape.

C. Assessment of observer performance

For each of the five visual tasks shown in Figure 2, we have evaluated human observer performance for standard B-mode and Wiener-filtered envelope images through psychophysical studies. We compare these to Monte-Carlo studies of the ideal observer acting on RF data and Smith-Wagner approximations to the ideal observer acting on envelope images.

We assessed human-observer detection and discrimination performance through two-alternative forced-choice (2AFC) experiments [32] in which a stimulus generated under hypothesis H_1 and an independent stimulus generated under hypothesis H_2 are presented to the observer, and the observer's task is to identify the stimulus generated from H_2, the hypothesis of malignant tissue. For the ideal observer, the stimuli were sampled RF data. For human observer studies and for the Smith-Wagner model observers, the stimuli were B-mode and Wiener-filtered envelope images.

For the ideal observer, 6400 pairs of RF echo frames were generated for each task. If we let $\mathbf{g}_{1,i}$ be the RF frame from H_1 in the ith trial and $\mathbf{g}_{2,i}$ be the RF frame from H_2, then the trial score, o_i, is given by

$$o_i = \text{step}\left(\lambda\left(\mathbf{g}_{2,i}\right) - \lambda\left(\mathbf{g}_{1,i}\right)\right),$$

where the step function (also referred to as a Heaviside function) assumes a value of 1 for positive arguments and zero for negative. Hence, the score is 1 if the observer response is greater for $\mathbf{g}_{2,i}$ than $\mathbf{g}_{1,i}$. This corresponds to the observer correctly choosing the image generated under H_2.

With human observers, we obtain the score in each trial directly by showing malignant and benign images side by side randomizing which side the images appear on so that they are independent from trial to trial. We record each observer's choice of the image representing “malignancy” (H_2). When an observer correctly identifies the image from the malignant class, the score for that observer in that trial is 1. Trials in which the observer misidentifies a benign image as malignant result in a score of 0.

The proportion of correct responses, P_c, is defined as the expectation of the trial score. Under general assumptions, P_c is equivalent to area under the ROC curve (AUC) and is monotonically related to the detectability index [25],

$$d_A = \sqrt{2}\Phi^{-1}(P_c) = 2\text{erf}^{-1}\left(2\text{AUC} - 1\right), \tag{16}$$

where Φ^{-1} is the inverse cumulative normal function and erf^{-1} is the inverse error function. Proportion correct is estimated from the average score over all trials in an experiment.

To compute the efficiency of a human observer with respect to the ideal observer, the object contrast factor in each task is adjusted to handicap the ideal observer performance until it matches that of the human observer [33]. If we define C_H as the object contrast factor for the human-observer study, and C_I as the parameter setting that produces equivalent performance in the ideal observer ($d_{A\text{-}Human} = d_{A\text{-}Ideal}$), then the observer efficiency with respect to the ideal observer is given by

$$\eta = 100\% \times \left(\frac{C_I}{C_H}\right)^2. \quad (17)$$

Efficiency can also be computed as the square of the detectability index of the human observer divided by that of the ideal observer at the same contrast as the human observer study [33]. However, the detectability index of the ideal observer at the object contrasts used for the psychophysical experiments is usually so high that it is very difficult to accurately estimate by the 2AFC procedure. Hence we favor the efficiency computation of Equation 17.

D. Psychophysical studies

Human-observer performance was assessed through 2AFC psychophysical studies. A total of 6 observers participated in a total of 10 studies investigating each of the 5 tasks with both B-mode and Wiener-filtered data. Two of the observers are authors of this work (CA and MI) and the remaining four observers consisted of graduate students, fellows, and researchers not directly related to the project. Simple tasks with tightly controlled stimuli of the sort reported here do not require extensive medical experience to perform, and nonclinical observers (trained for specific tasks) appear to perform equally well in such cases as those with clinical training [34,35].

Pilot studies on independent sets of images were used to find object contrast factors such that human observer performance in the B-mode images would be approximately 80% correct. This level of performance yields a relatively low coefficient of variation in 2AFC studies [36], and leaves a reasonable range for improved performance in the Wiener-filtered envelope images. Since the primary goal of the psychophysical studies was to investigate the effect of Wiener-filtering the RF data before computing an envelope image, in each task, B-mode and Weiner-filtered images were generated from the same RF frame data, thereby controlling for case variability [37]. All observers scored both the B-mode and Wiener-filtered studies, to control for observer effects. The order of the tasks was randomized for each observer, and within each task the order of the Wiener-filtered study and the B-mode study was also randomized to reduce any order effects.

Before each task began, observers completed 100 trials of training that began with 10 trials at very high contrast, through two sets of 20 trials at progressively harder parameter settings and finally 50 trials at the parameter setting of the actual study. Training responses were not used to assess observer performance. Immediately after training, the observers scored 400 2AFC trials that determined their observed performance in the task. The studies were performed in a darkened room on a calibrated monochrome monitor (Image Systems, Minnetonka, MN) using a perceptually linearized [38] lookup table over a luminance range of 0.5 to 150Cd/m^2. The monitor pixel size was .3mm. Viewing distance was not controlled, but generally observers maintained a comfortable viewing distance of approximately 40–50cm. At 40cm viewing distance, the 5mm lesion size in tasks 2–5 subtends a visual angle of 1.7°.

IV. RESULTS AND DISCUSSION

A. Human observer performance

Figure 5 charts the performance of the human observers as determined in the psychophysical studies. The chart gives proportion correct averaged across the six observers in each of the five tasks for B-mode and Wiener-filtered envelope images. The average values in each condition are given in Table 1, along with a paired-comparisons *t*-test between B-mode and Wiener-filtered images for each task. Pilot studies were used in to determine the parameter settings needed to get approximately 80% correct in the B-mode image experiments.

The B-mode average performance values in Table 1 show that the pilot studies appear to have been reasonably accurate, with the largest deviation from 80% correct coming in Task 1, where the average performance is off by 5.4 percentage points. Table 1 also shows a substantial increase in performance with the Wiener-filtered images for Tasks 1–4. Tasks 2 and 3 increase by approximately 10 percentage points while tasks 1 and 4 increase by as much as 16 percentage points. The paired-comparison *t*-test shows that these increases are significant at the $\alpha = 0.01$ level. It is also worth noting that every observer improved performance in each of these tasks on the Wiener-filtered images.

But notably, performance went down in Task 5 for Wiener-filtered images relative to the B-mode images. Table 1 shows that the significance of this difference is slightly greater than the $\alpha = 0.01$ level.

B. Ideal observer performance

The results of the Monte-Carlo studies of ideal observer performance are plotted in Figure 6. The plots in Figure 6A–E give performance in terms of the detectability index (d_A as defined in Equation 11) as a function of object contrast. Recall from Equation 6 that the ideal observer acts on RF frames. Shown for comparison are performance curves for the Smith-Wagner observer, Equation 14, acting on the B-mode and Wiener-filtered envelope images. Note that in Task 1, performance of the ideal observer and the Smith-Wagner observer for Wiener-filtered envelope images were identical (i.e. the power series has effectively converged after 1 iteration), and so only the ideal observer plot is given. For reference, the average detectability of the human observers is also given at the object contrast used in the experiments. In Figure 6A, we notice that d_A for the Smith-Wagner approximation in task 1 is approximately proportional to contrast as they predicted for low-contrast lesion detection [6]. The ideal observer's performance is also linear with contrast, yet the slope is greater suggesting that RF data provide more task 1-relevant information.

The ideal observer performance is plotted after 10 iterations of the power series for inversion of the nonstationary covariance matrix. At 10 iterations, the detectability index was improving by less than 1–2% per iteration. Running on a PC (Processor speed 866MHz, 500Mb RAM), each plot took 8–10 hours of CPU time to generate.

In Tasks 1, 2, 3, and 5, the detectability index of the ideal observer is seen to be reasonably linear as a function of object contrast. This would indicate that efficiency with respect to the ideal observer as defined in Equation 17 is equivalent to efficiency computed as a ratio of d_A values squared. However, in Task 4, the ideal observer performance curve appears to have a decelerating nonlinearity for object contrasts near zero. In this task, the efficiency computed from the ratio of detectability index values at equal contrasts will not necessarily equal the efficiency computed from the ratio of object contrasts at equal detectability.

Figure 6F gives shows graphically how the efficiency with respect to the ideal observer in Equation 17 is calculated. The intersection of a horizontal line at the level of the human

observer performance with the ideal observer curve is used to determine the contrast needed for the ideal observer to achieve equivalent performance. The efficiency is then given as the ratio of this contrast to that of the human observer data squared. This approach can also be used to determine the relative efficiency with respect to the Smith-Wagner observer.

C. Observer Efficiency

Human observer efficiency in the visual tasks is plotted in Figure 7A. Note that the relatively uniform proportion correct values for B-mode images (Figure 5) does not result in uniform efficiency. Here we see approximately two orders of magnitude difference in efficiency going from the highest efficiency B-mode task (Task 1) to the lowest (Task 4). Efficiency for the Wiener filtered data is substantially higher for Tasks 1–4 by factors ranging from 2.5 to more than 20. Task 5 exhibits approximately a factor of 2 drop in efficiency. Efficiency for the Wiener filtered images ranges from 44% in Task 1 to as low as 0.36% in Task 5. The relatively high detection efficiency of human observer in Task 1 reproduces the results of earlier studies utilizing low-contrast lesion detection tasks. For example, Insana and Hall [30] found observer detection efficiencies near 60% and Abbey et al [8] found efficiencies between 40% and 60%.

Given the large range of observer efficiency across the various tasks and the substantial differences between B-mode and Wiener-filtered envelope images, it is of interest to understand the sources of inefficiency in our human observer data. From the perspective of information transfer, we would like to know where the diagnostic information being used by the ideal observer is lost. Is the information being lost in the computation of an envelope image, or is the information lost because of limitations in the human eye-brain system? We use the Smith-Wagner test statistic defined in Equation 14 to approximate ideal performance for envelope images, with and without Wiener filtering, as a means to gain insight into this issue.

Consider for the moment task performance using envelope images. Let $\eta_{H|SW}$ be the relative efficiency of the human observer with respect to the Smith-Wagner approximation. This relative efficiency is found as described in Figure 6F, except that the performance curve of the Smith-Wagner observer is used instead of the RF ideal observer. Now let η_{SW} be the efficiency of the Smith-Wagner observer with respect to the ideal observer acting on RF frame data. We can decompose the human observer efficiency into the product,

$$\eta_H = \eta_{SW}\eta_{H|SW} \cdot \tag{18}$$

The η_{SW} term measures the information lost in creating a envelope image while the $\eta_{H|SW}$ term measures the information lost by the human observer. This same process can be used with the Wiener-filtered envelope images. Thus we can disambiguate the information lost in these two steps. However, it should be noted that this analysis relies on the assumption that the Smith-Wagner ideal observer is equivalent to the ideal observer restricted to using an envelope image. Since the ideal observer always maximizes performance, the Smith-Wagner observer must therefore be a lower-bound for an envelope-image ideal observer. Here we assume that this lower bound is tight (i.e. that performance of the Smith-Wagner observer is very nearly as good as the ideal observer). If the Smith-Wagner observer substantially under-estimates the performance of the envelope image ideal observer, our analysis will over-estimate the information lost in creating an envelope image, and thus underestimate the information lost by the human observers.

The efficiency of the Smith-Wagner observer is given in Figure 7B, and the relative efficiency of the human observers to the Smith-Wagner approximation is given in Figure 7C. These plots reveal some surprising effects. For example, the low efficiency of human

observers in Task 4 can be almost entirely explained as a loss of information in the computation of an envelope. Another surprise is the high relative efficiency of human observer for the B-mode images as compared to Wiener-filtered images as seen in Figure 7C. Figure 7B suggests that Wiener-filtered envelope images contain much more diagnostic information than non-filtered images, at least for tasks 1–4, but that human observers do not have full access to the additional information. Nevertheless, human visual detection efficiency is significantly improved by Wiener filtering of the RF data. If this result is borne out by further investigation, is suggests that further improvements in detection performance may be found by subsequent processing of the Wiener-filtered data in a manner reminiscent to color-flow Doppler imaging of blood velocity. Here, the RF echo signal contains information about blood cell movement, but B-mode images do not make this information easily accessible to humans. Consequently echo signals are processed to estimate velocity, and the estimates are rendered in color to clearly indicate flow information.

It is also possible that the differences in observer efficiencies shown in Figure 7B for tasks 2–4 could be explained by a breakdown in the Smith-Wagner observer, where the assumptions of large, constant target contrast is violated. Violations will reduce the performance of Equation 14 below ideal, so that the human detection efficiencies summarized in Figure 7C would be smaller than those indicated. The only way to test this definitively would to find the ideal observer of B-mode images for two-class discrimination tasks limited by spatial resolution.

The efficiency of the Smith-Wagner observers also explains much of the impaired performance of human observers in Task 5 when Wiener-filtered envelope images are used. Recall that this task involves the discrimination of an anechoic lesion from a weakly scattering hypoechoic one. This performance degradation may reflect the fact that the Wiener filter is not tuned for the lesion interior, where the object scattering function is significantly lower than the highly scattering tissue surrounding it. As a result, the Wiener filter will tend to boost frequencies in which the signal is much noisier than assumed in the derivation of the Wiener filter.

The decomposition in Equation 18 used for this analysis is useful for ultrasonic imaging in that it separates the effects of signal processing from those of the human observer. However, a number of interesting questions remain to be answered regarding sources of information loss within the human observer. These have all been lumped into the $\eta_{H|SW}$ term here. Known limitations of human observers such as sampling efficiency [39], internal noise [40] and nonlinear effects such as spatial uncertainty [41, 42] remain to be investigated for their role in limiting human observer efficiency.

D. Assumptions and limitations of the study

The ideal observer has been derived under a number of assumptions about the nature of scattering in breast tissue, and about the form of the system response. Here we review those assumptions and discuss their ramifications briefly.

We have assumed that the scattering function for tissue can be represented by a white Gaussian random process. Tissues that are better described as very sparse random distributions of point scatterers, e.g., cysts, or nonrandom distributions, e.g., cellular hyperplasia, may lead to non-Gaussian statistics in the RF response, as described previously [43,7] and more recently by Barrett and Myers [25, Chapter 18]. We would expect the advantage of Wiener filtering to diminish as the density of point scatterers is reduced under high echo signal-to-noise ratio (eSNR) conditions. When the density of scatterers is low enough that the pulse interacts with only one scatterer at any given time, the ideal observer will simply count the individual scatterers and find results that are independent of any

filtering. However, if the density of scatterers is sparse and eSNR is low, then the Wiener filter responds as a matched filter for the point spread function, and some improvement may be expected through noise suppression. Also, it is possible that the approximation to the covariance matrix inverse in Equation 10 may require many terms to converge in this situation, and therefore the Wiener filter may be a poor approximation to the ideal strategy, as seen to some extent in Figure 6.

The second part of the independent Gaussian assumption for **f** in Equation (2) is the assumption that the correlation length among object scatterers is small with respect to the pulse wavelength. This seems reasonable for scattering at the cellular scale where the wavelength is 0.15 mm at 10 MHz and cell size is on the order of 0.015 mm. However, it may be the case that scattering arising from vasculature and other macrocellular tissue objects generates extended object correlations The approach taken in this paper can be generalized to incorporate a stationary correlation structure by replacing the object covariance matrix, defined above as σ^2_{obj} (**I**+**S**), by

$$\sigma^2_{\text{obj}}\,(\mathbf{I}+\mathbf{S})^{1/2}\,\mathbf{C}_{\text{obj}}\,(\mathbf{I}+\mathbf{S})^{1/2},$$

where $\mathbf{C}_{\text{obj}}$ is a stationary matrix of correlation coefficients. A power series approach to computing the ideal observer can be derived from this generalization. However, it is not clear that the same spatial correlation structure will exist inside a well defined lesion as in the surrounding tissue, and hence it is not clear that this generalization would fully resolve the issue of spatial correlations in the object scattering function.

The assumption of shift-invariance in the system response to the pulse profile is, at best, only reasonable in a small area. It also ignores conditions that generate strong grating lobes, e.g., those generated when a phased array is electronically steered at large angles. Hence in order to be applicable in a large-area image, the Wiener-filter must be applied locally and the impulse response updated for each isoplanatic region. Wave front distortions, such as phase aberrations and acoustic shadowing, may be reconsidered as shift-varying impulse responses. Shift variance does not invalidate the ideal observer concept as summarized by Eq (5) – Eq (8), but it does invalidate the linear approximation of Eq (9) that allows for closed form results and straightforward interpretation.

While this work has made a number of simplifying assumptions in order to derive a tractable computational model, we feel that the results still have a bearing on the more complex clinical domain. Our results suggest that relevant information about features important to the classification of disease can be transferred to the diagnostic image with much greater efficiency when the recorded RF signal is subjected to judicious processing.

V. SUMMARY AND CONCLUSIONS

The central conclusion this work is that there appears to be considerably more diagnostic information in the measured RF signal acquired by an ultrasound transducer than in the final B-mode envelope image, and, in some cases, a substantial quantity of this information can be recovered by Weiner-filtering the RF signal before computing an envelope. We demonstrate this through a combination of ideal observer analysis and psychophysical studies on a panel of tasks investigating features related to discriminating malignant and benign tissue in ultrasound mammography, although the approach is not limited to this application.

Our ideal observer analysis is based on Gaussian assumptions for the scattering function of tissue established in previous work. For two-class discrimination tasks these Gaussian assumptions lead to an ideal observer decision variable that is a quadratic form involving the inverse covariance matrix for each class. We have further developed the methodology in this area by deriving an iterative algorithm for implementing power-series inversion of the large nonstationary covariance matrices needed to implement the ideal observer. Each iteration of this algorithm is equivalent to adding another term in the power-series expansion. An analysis of the power-series expansion after one iteration reveals a role for the Wiener filtering before computing the final envelope image.

We have investigated the effects of Wiener filtering on a panel of five tasks that investigate features of ultrasound images used by mammographers to discriminate benign from malignant tissue in the breast. We find that in four of the five tasks, Wiener filtering results in a substantial improvement in observer performance over the standard B-mode envelope. These tasks include detection of a mildly hypoechoic region, and three tasks that investigate the shape and appearance of lesion boundaries. However, in a task involving discrimination of a hypoechic lesion interior from an anechoic interior, we find a reduction in performance after Wiener filtering. We suggest that this reflects an inappropriate amplification of noise by the Wiener filter in the lesion interior.

We find a large variability in observer efficiency with respect to the ideal observer with more than two orders of magnitude difference between the highest and lowest measured efficiency values across the five tasks. For the purpose of optimizing ultrasonic signal processing, it is of interest to know if low efficiency of human observers reflects a loss of diagnostic information in the computation of an envelope image, or if the information is available in the images but inaccessible to human observers. We have used an approximation to the ideal observer acting on an envelope image developed by Smith and Wagner to disambiguate effects of computing an envelope from those of the human observer. This analysis shows that the envelope computation is the more significant limiting step for standard B-mode processing, and is generally improved by Wiener-filtering the RF data. Surprisingly, human observers appear to be less efficient at reading the Wiener-filtered envelope images than the B-mode images making the overall gains in performance even more impressive. The residual inconsistency in human observer efficiencies for these tasks motivates further study investigating its source as well as the development of observer models for predicting the human observer.

APPENDIX

In this appendix, we show that the iterative algorithm given in Equation 11 is equivalent to the power series inversion formula given in Equation 10. Specifically we show that the final product, $\mathbf{v}_0^t\mathbf{v}_K$, is equivalent to the first K elements of the power series,

$$\mathbf{v}_0^t\mathbf{v}_k=\mathbf{g}^t\boldsymbol{\Sigma}_0^{-1/2}\sum_{k=0}^{K}\left(-\boldsymbol{\Sigma}_0^{-1/2}\boldsymbol{\Delta\Sigma}_i\boldsymbol{\Sigma}_0^{-1/2}\right)^k\boldsymbol{\Sigma}_0^{-1/2}\mathbf{g}\,. \tag{A1}$$

We use induction to demonstrate this relation, and therefore we need to show that the relation holds for $K = 0$, and that it holds for $K + 1$ if it holds at K.

For $K = 0$, the right side of Equation A1 simplifies to

$$\mathbf{g}^t\boldsymbol{\Sigma}_0^{-1}\mathbf{g} \tag{A2}$$

since a matrix raised to the power zero is defined to be the identity and $\boldsymbol{\Sigma}_0^{-1/2}\boldsymbol{\Sigma}_0^{-1/2}=\boldsymbol{\Sigma}_0^{-1}$. This is also precisely what the algorithm gives since $\mathbf{v}_0$ is initialized to $\boldsymbol{\Sigma}_0^{-1/2}\mathbf{g}$, and hence $\mathbf{v}_0^t\mathbf{v}_0=\mathbf{g}^t\boldsymbol{\Sigma}_0^{-1}\mathbf{g}$.

We begin the second step in the induction by considering the vector $\mathbf{u}_K$. From the update formula for $\mathbf{u}$ given in Equation 11, it is clear that

$$\mathbf{u}_K=\left(-\boldsymbol{\Sigma}_0^{-1/2}\Delta\boldsymbol{\Sigma}_i\boldsymbol{\Sigma}_0^{-1/2}\right)^K\boldsymbol{\Sigma}_0^{-1/2}\mathbf{g}\,. \tag{A3}$$

Now, let us assume Equation A1 holds for some step K, and consider $K+1$. In this case, the iterative algorithm specifies that

$$\mathbf{v}_0^t\mathbf{v}_{K+1}=\mathbf{v}_0^t\left(\mathbf{v}_K+\mathbf{u}_{K+1}\right). \tag{A3}$$

Using Equation A1 and Equation A3 above we find that

$$\begin{aligned}\mathbf{v}_0^t\mathbf{v}_{K+1} &=\mathbf{g}^t\boldsymbol{\Sigma}_0^{-1/2}\sum_{k=0}^{K}\left(-\boldsymbol{\Sigma}_0^{-1/2}\Delta\boldsymbol{\Sigma}_i\boldsymbol{\Sigma}_0^{-1/2}\right)^k\boldsymbol{\Sigma}_0^{-1/2}\mathbf{g}\\ &\quad+\mathbf{g}^t\boldsymbol{\Sigma}_0^{-1/2}\left(-\boldsymbol{\Sigma}_0^{-1/2}\Delta\boldsymbol{\Sigma}_i\boldsymbol{\Sigma}_0^{-1/2}\right)^{K+1}\boldsymbol{\Sigma}_0^{-1/2}\mathbf{g}\\ &=\mathbf{g}^t\boldsymbol{\Sigma}_0^{-1/2}\sum_{k=0}^{K+1}\left(-\boldsymbol{\Sigma}_0^{-1/2}\Delta\boldsymbol{\Sigma}_i\boldsymbol{\Sigma}_0^{-1/2}\right)^k\boldsymbol{\Sigma}_0^{-1/2}\mathbf{g},\end{aligned} \tag{A4}$$

and thus A1 holds for $K+1$. We have therefore shown by induction that iterating the algorithm of Equation 11 successively adds terms to the power series inversion formula.

Acknowledgments

The authors thank Huini Du, Yongfeng Yang, Gregory Stanczak, and Douglas Stephens for participating in the psychophysical studies.

This work was supported in part by the U.S. National Institutes of Health under Grants R01-CA082497 and R21-CA102733.

REFERENCES

1. Barrett HH. Objective assessment of image quality: effects of quantum noise and object variability. J Opt Soc Am A. 1990; 7(7):1266–1278. [PubMed: 2370589]
2. Wagner RF, Barrett HH. Quadratic tasks and the ideal observer. Proc. SPIE. 767:1–4.
3. Wagner RF. Low contrast sensitivity of radiologic, CT, nuclear medicine and ultrasound medical imaging systems. IEEE Trans. Med. Imag. 1983; vol MI-2:105–121.
4. Barrett HH, Abbey CK, Clarkson' E. Objective assessment of image quality. III. ROC metrics, ideal observers, and likelihood-generating functions. J Opt Soc Am A. 1998; 15(6):1520–1535.
5. Wagner RF, Smith SW, Sandrik JM, Lopez H. Statistics of speckle in ultrasound B-scans. IEEE Trans. Sonics Ultrason. 1983; vol. SU-30:156–163.
6. Smith SW, Wagner RF, Sandrik JM, Lopez H. Low-contrast detectability and contrast/detail analysis in medical ultrasound. IEEE Trans. Sonics Ultrason. 1983; vol. SU-30:156–163.
7. Wagner RF, Insana MF, Brown DG. Statistical properties of medical ultrasound with applications to medical ultrasound. J. Opt. Soc. Am. A. 1987; vol. 4:910–922. [PubMed: 3298583]
8. Abbey CK, Zemp RJ, Insana MF. Pre-envelope deconvolution for increased lesion detection in ultrasonic imaging. Proc. SPIE. 2003; 5034:280–288.
9. Zemp RJ, Abbey CK, Insana MF. Linear System Models for Ultrasonic Imaging: Application to Signal Statistics. IEEE Trans. UFFC. 2003; 50(6):642–654.

10. Zemp RJ, Abbey CK, Insana MF. Detection performance theory for ultrasound imaging systems. IEEE Trans. Med Imag. 2004; 24(3):300–310.
11. Abbey, CK.; Zemp, RJ.; Liu, J.; Insana, MF. Observer efficiency in discrimination tasks simulating malignant and benign breast lesions with ultrasound. Proc IEEE Signal Proc.; Asilomar, CA. 2004 November.
12. Brunke SS, Insana MF, Dahl JJ, Hansen C, Ashfaq M, Ermert H. An ultrasound research interface for a clinical system. IEEE Trans UFFC. (submitted July 2005).
13. O'Donnell M. Coded excitation systems for improving the penetration of real-time phased array imaging systems. IEEE Trans UFFC. 1992; vol. 39(3):341–351.
14. American College of Radiology. Breast Imaging Reporting and Data System Atlas. Reston, Va: 2003.
15. Bassett LW, Kimme-Smith C. Breast sonography. Am J Roentgenol. 1991; 156(3):449–455. [PubMed: 1899737]
16. Zonderland HM, Coerkamp EG, Hermans J, van de Vijver MJ, van Voorthuisen AE. Diagnosis of breast cancer: contribution of US as an adjunct to mammography. Radiology. 1999; 213(2):413–422. [PubMed: 10551221]
17. Kolb TM, Lichy J, Newhouse JH. Comparison of the performance of screening mammography, physical examination, and breast US and evaluation of factors that influence them: an analysis of 27,825 patient evaluations. Radiology. 2002; 225(1):165–175. [PubMed: 12355001]
18. Kolb TM, Lichy J, Newhouse JH. Occult cancer in women with dense breasts: detection with screening US--diagnostic yield and tumor characteristics. Radiology. 1998; 207(1):191–199. [PubMed: 9530316]
19. Crystal P, Strano SD, Shcharynski S, Koretz MJ. Using sonography to screen women with mammographically dense breasts. Am J Roentgenol. 2003; 181(1):177–182. [PubMed: 12818853]
20. Wagner RF, Barrett HH. Quadratic tasks and the ideal observer. Proc. SPIE. 1987; vol. 767:306–309.
21. Fatemi M, Kak AC. Ultrasonic B-scan imaging: theory for image formation and a technique for image restoration. Ultrasonic Imaging. 1980; 2:1–47. [PubMed: 7189615]
22. Jensen JA. Deconvolution of ultrasound images. Ultrasonic Imaging. 1992; 14:1–15. [PubMed: 1549893]
23. Insana, MF.; Brown, DG. Acoustic scattering theory applied to soft biological tissues. In: Shung, KK.; Thieme, GA., editors. Ultrasonic Scattering in Biological Tissues. Boca Raton: CRC Press; 1993.
24. Whalen, AD. Detection of Signals in Noise. San Diego: Academic Press; 1971.
25. Barrett, HH.; Myers, KJ. Foundations of Image Science. Hoboken New Jersey: John Wiley & Sons; 2004.
26. Gonzalez, RC.; Woods, RE. Digital Image Processing. Reading MA: Addison-Wesley; 1993.
27. Golub, GH.; Van Loan, CF. Matrix Computations. third edition. Johns Hopkins; 1996.
28. Pratt, WK. Digital Image processing. 3rd Edition. Hoboken New Jersey: John Wiley & Sons; 2001.
29. Goodman, JW. Statistical properties of laser speckle patterns. In: Dainty, JC., editor. Laser Speckle and Related Phenomena. Berlin: Springer-Verlag; 1975.
30. Insana MF, Hall TJ. Visual detection efficiency in ultrasonic imaging: a framework for objective assessment of image quality. J. Acoust. Soc. Am. 1994; 95:2081–2090.
31. Du H, Liu J, Pellot-Barakat C, Insana MF. Optimizing multicompression approaches to strain imaging. IEEE Trans Ultrason Ferro Freq Contrl. (in press).
32. Green, DM.; Swets, JA. Signal Detection Theory and Psychophysics. NY: Wiley; 1966.
33. Tanner, WP.; Birdsall, TG. Definitions of d' and η as psychophysical measures. In: Swets, JA., editor. Signal Detection and Recognition by Human Observers: Contemporary Readings. NY: Wiley; 1964.
34. Eigler NL, Eckstein MP, Mahrer KN, Whiting JS. Improving detection of coronary morphological features from digital angiograms. Effect of stenosis-stabilized display. Circulation. 1994; vol. 89(6):2700–2709. [PubMed: 8205684]

35. Burgess AE, Jacobson FL, Judy PF. Human observer detection experiments with mammograms and power-law noise. Med Phys. 2001; vol. 28(4):419–437. [PubMed: 11339738]

36. Burgess AE. Comparison of receiver operating characteristic and forced choice observer performance measurement methods. Med Phys. 1995; vol. 22(5):643–655. [PubMed: 7643805]

37. Roe CA, Metz CE. Variance-component modeling in the analysis of receiver operating characteristic index estimates. Acad Radiol. 1997; vol. 4(8):587–600. [PubMed: 9261459]

38. Krupinski EA, Roehrig H. The influence of a perceptually linearized display on observer performance and visual search. Acad Radiol. 2000; 7(1):8–13. [PubMed: 10645452]

39. Eckstein MP, Ahumada AJ, Watson AB. Visual signal detection in structured backgrounds, II. Effect of contrast gain control, background variations and white noise. J Opt Soc Am A. 1997; vol 14:2406–2419.

40. Burgess AE, Colborne B. Visual signal detection. IV. Observer inconsistency. J Opt Soc Am A. 1988; vol. 5(4):617–627. [PubMed: 3404312]

41. Burgess AE, Ghandeharian H. Visual signal detection. II. Signal-location identification. J Opt Soc Am A. 1984; vol. 1(8):906–910. [PubMed: 6470843]

42. Pelli DG. Uncertainty explains many aspects of visual contrast detection and discrimination. J Opt Soc Am A. 1985; vol. 2(9):1508–1532. [PubMed: 4045584]

43. Jakeman E E. Speckle statistics with a small number of scatterers. Opt Eng. 1984; vol. 23:453–461.

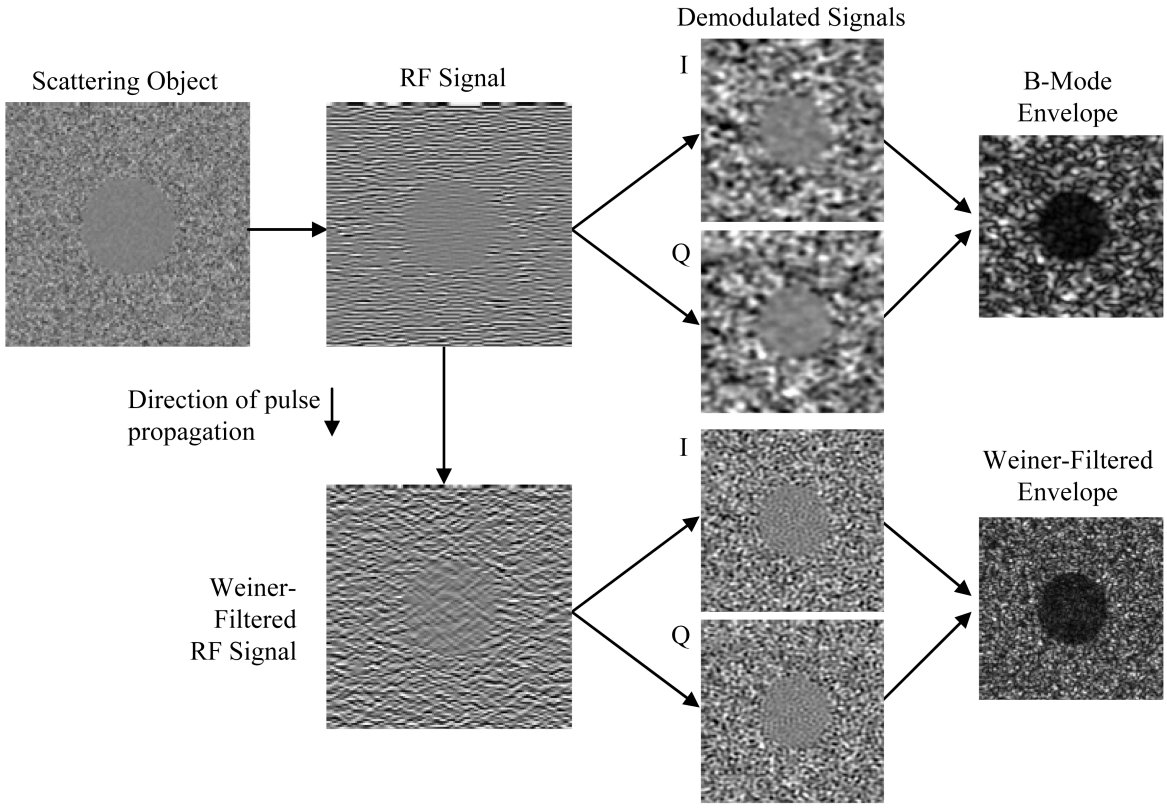

Fig. 1.

A graphical model of ultrasonic signal processing used in this work. The top row shows the formation of a standard B-Mode image including the object scattering function, the acquired radio-frequency (RF) frame, demodulated In-Phase (I) and Quadrature (Q) signals, and the final envelope image. Images of the demodulated signals and the final envelope images are reduced in size to indicate downsampling during demodulation. In this work we investigate the effect of implementing a Weiner-filter on the radio-frequency frame data. After Wiener filtering, the signal is demodulated and an envelope image is computed.

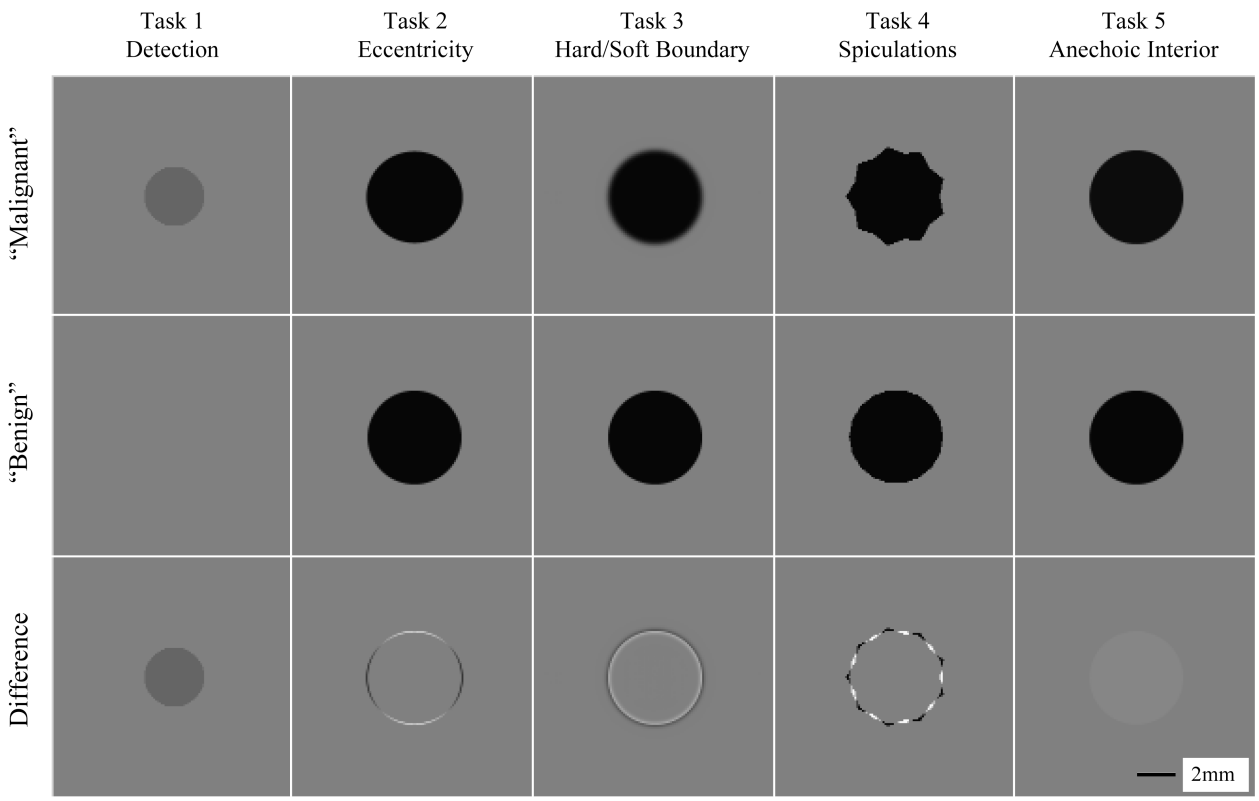

Fig. 2.

Variance profiles of "Malignant" and "Benign" scattering objects the 5 tasks. The third row is the difference in the variance profiles. In Task 1, the lesion is 3mm in diameter. In tasks 2–5 the lesion is approximately 5mm in diameter.

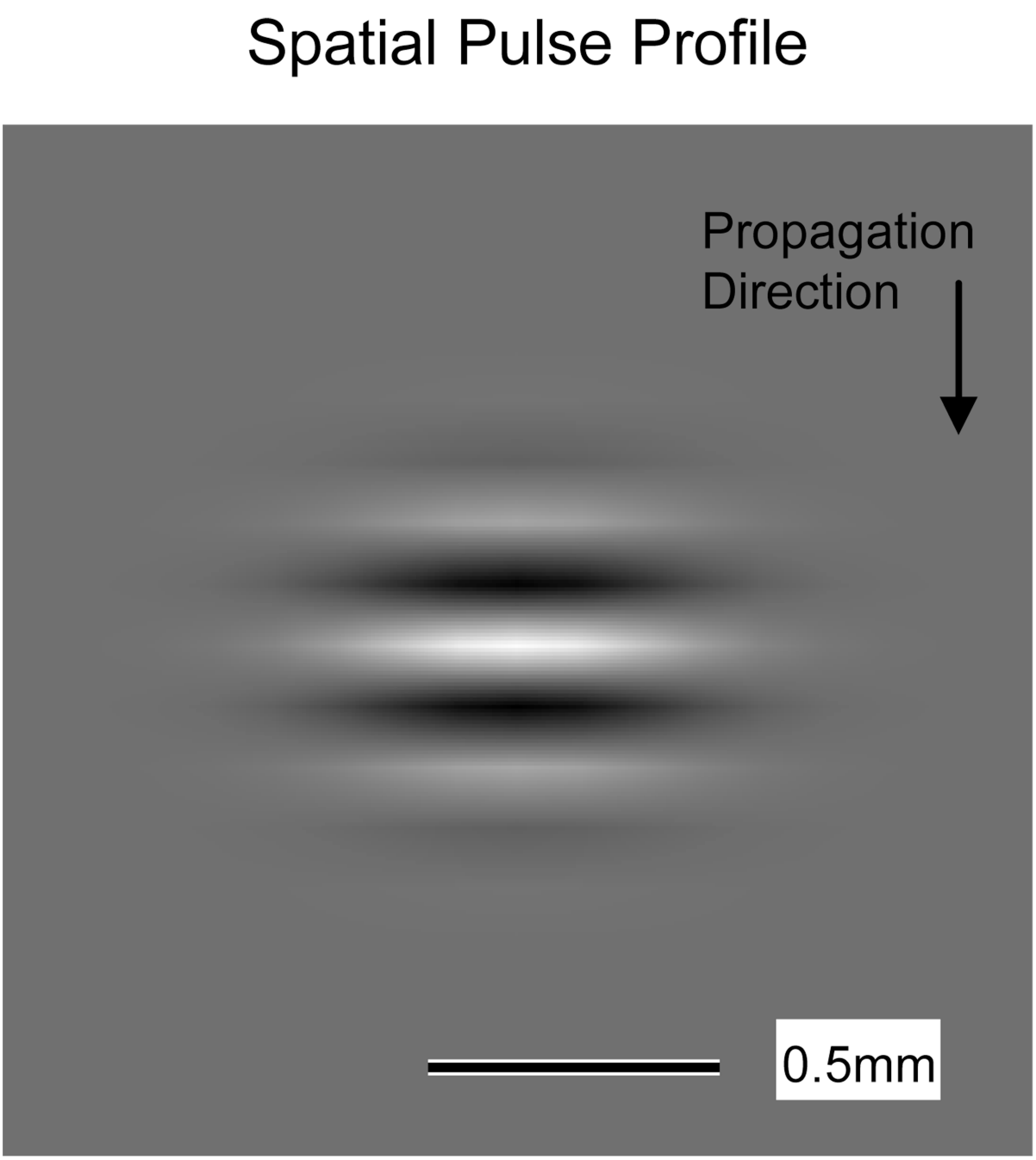

Fig. 3.
Pulse profile used to generate RF data.

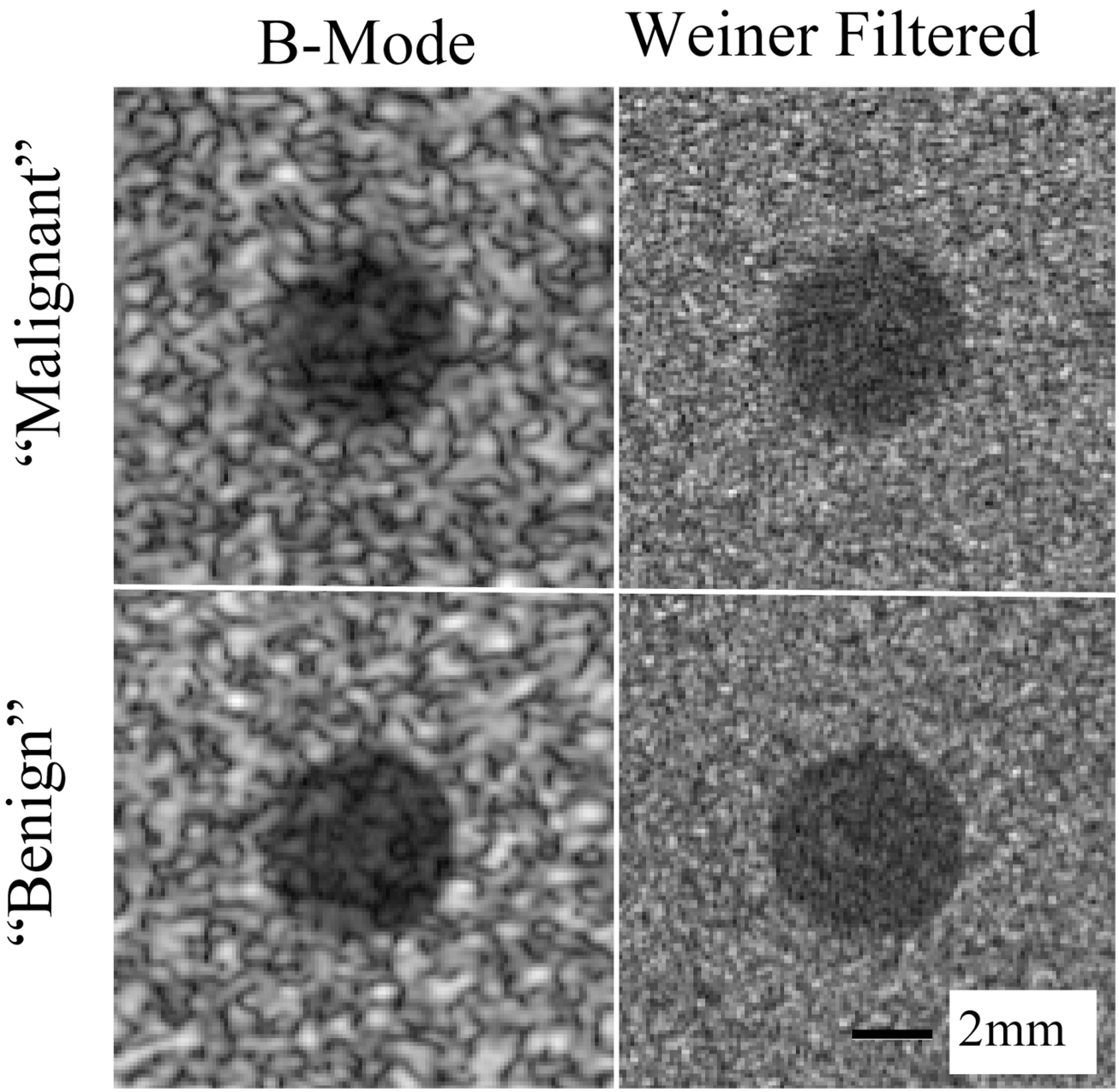

Fig. 4.
Examples of noisy B-mode and Wiener filtered images for Task 3 (at exaggerated contrast for display clarity).

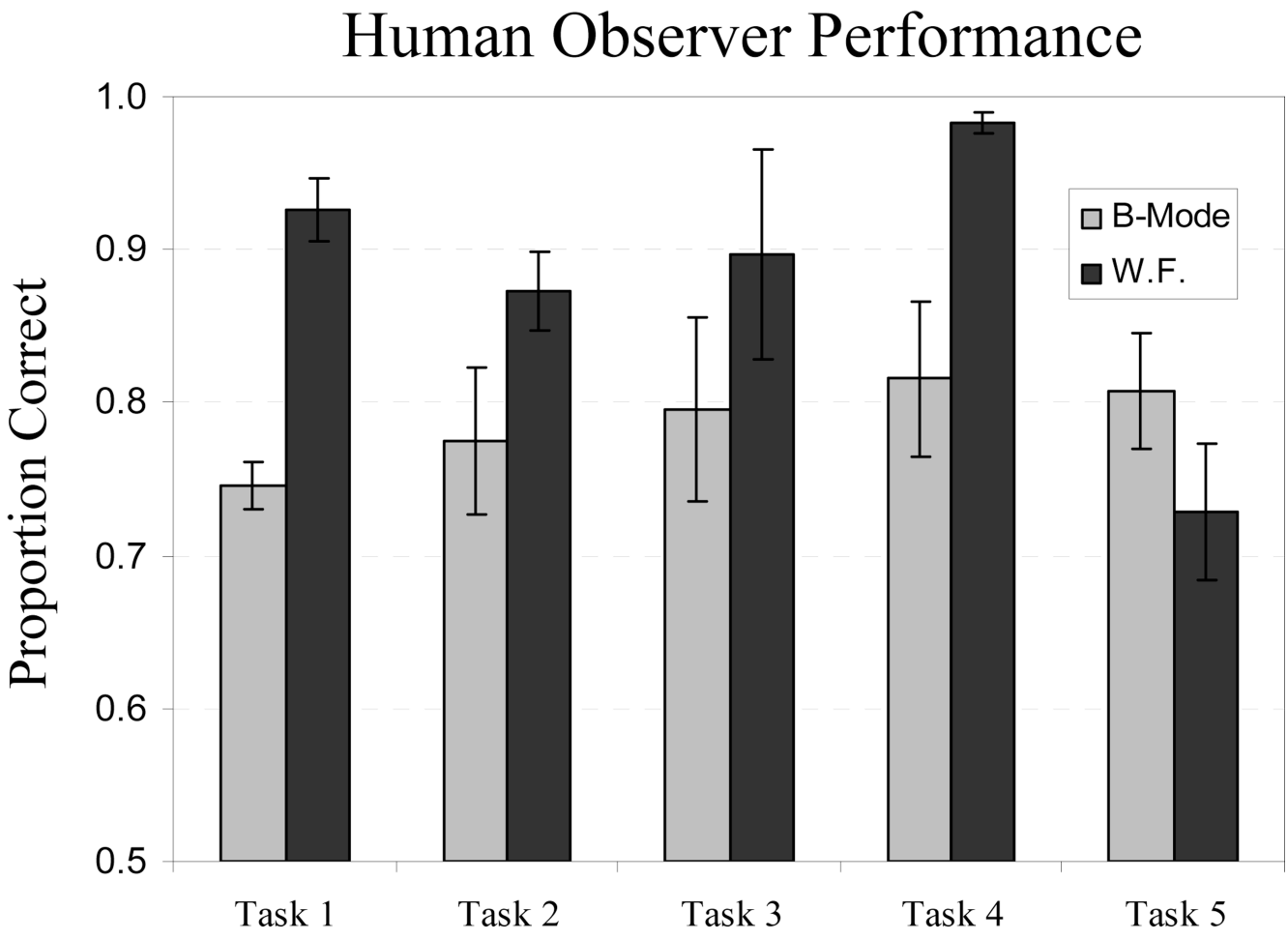

Fig. 5.
Human observer performance for B-mode and Weiner-filtered envelope images. Proportion correct in 2AFC psychophysical experiments are given for each of the five tasks. Error bars represent 95% confidence intervals about the mean across the six observers.

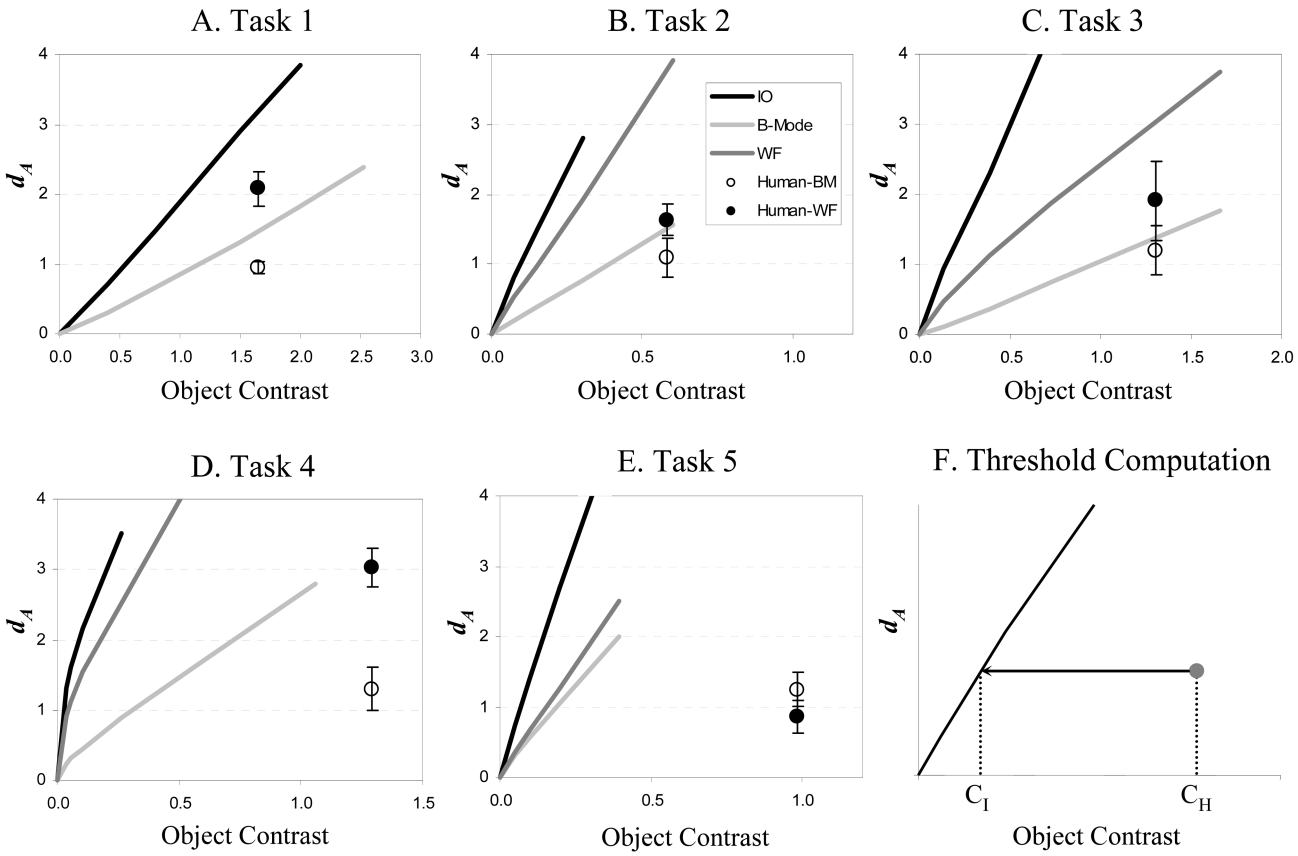

Fig. 6.

The detectability index d_A is plotted as a function of object contrast for the ideal observer derived from Monte-Carlo studies in parts A–E. The legend in Task 2 applies to all plots. Also plotted are the Smith-Wagner approximations for B-Mode and Weiner filtered (WF) envelope images, as well as average human observer performance (error bars represent +/−1 standard deviation across observers). Part F shows how visual detection efficiency is computed. We find the threshold contrast, C_I, that gives the same detectability index for the Ideal observer as the human observers at contrast C_H. Contrast values are combined to compute efficiency in Equation 17.

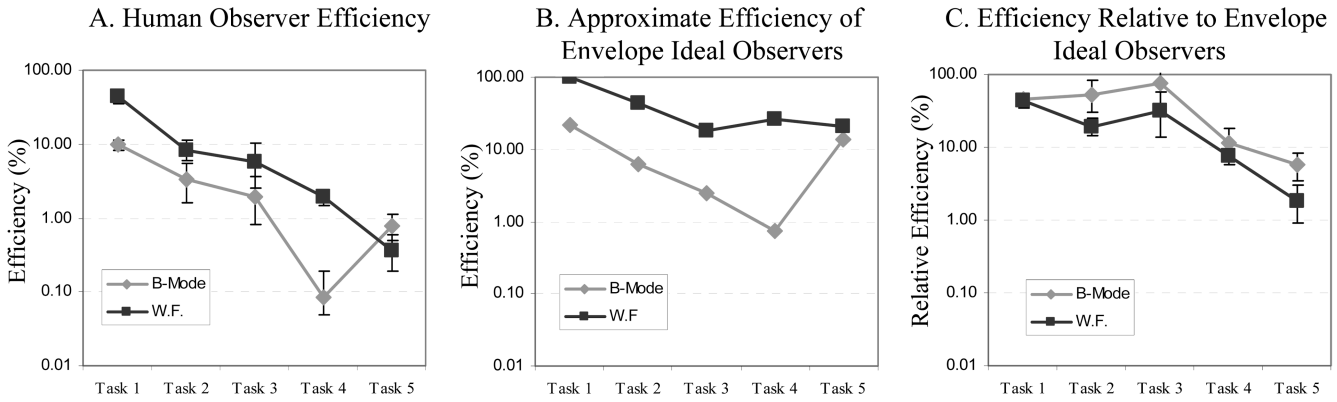

Fig. 7.

Efficiency Data. Human observer efficiency in both Wiener-Filtered and B-Mode images is plotted in A. To better understand the sources of inefficiency in A, the efficiency of the B-Mode and Wiener-Filtered Envelope Smith-Wagner (SW) observers are given in B. The relative efficiency of human observers to the SW are given in C.

TABLE I

Average Human Observer Performance

Task	B-Mode	W. F.	P-value
1	74.6%	92.7%	0.0000
2	77.5%	87.3%	0.0019
3	79.5%	89.7%	0.0016
4	81.5%	98.3%	0.0008
5	80.8%	72.9%	0.0115

Average percent correct across observers in each condition is given along with the p-value of a paired comparison *t*-test (df = 5, 2-tailed) between B-Mode and Weiner filtered images.